1

Optical Fiber with Two-dimensional Materials Integration for Photonic and Optoelectronic Applications

Jin-hui Chen[1, 2] and Fei Xu[2]

[1] *Xiamen University, Institute of Electromagnetics and Acoustics, Siming South Road, Xiamen, 361005, China*
[2] *Nanjing University, College of Engineering and Applied Sciences, Xianlin Road, Nanjing, 210023, China*

1.1 Introduction

The booming development of long-haul optical communications has been built on the ultralow-loss optical fiber network. Inspired by the seminal study by Kao and Hockham [1] that the optical loss of silica fibers can be significantly mitigated by reducing the impurity concentrations, the invention of low-loss silica fibers (~20 dB/km) marked the debut of modern optical communications [2]. The standard optical fibers are mainly made of silica materials with concentric core and cladding structures. Since the fiber core has a higher refractive index than the encircling cladding, the optical fiber usually confines light field in the core region through the total internal reflection at the interface. With the advances in materials science and manufacturing, state-of-the-art optical fibers show a transmission loss of 0.154 dB/km, which means that the light signal intensity only suffers from half loss after propagating 20 km along the fiber [2]. While the optical fibers simply transmit the light signals in the optical communications system, they have also found extended applications in various fields, such as optical imaging, distributed sensing, fiber lasers, and nonlinear optics.

In the past 20 years, it has witnessed the great progress of fiber optics with the development of fundamental science and advanced technology. From microstructures, the one-dimensional (1D) photonic crystals are implemented to realize the fiber Bragg gratings, and later many other kinds of grating structures, such as long-period gratings and tilted fiber Bragg gratings, are proposed and demonstrated for the optical sensing and signal processing. The photonic crystal fibers (PCFs) are emerged with two-dimensional (2D) structures running along the fiber length. These unique photonic structures overcome the limitations of total internal reflection principle and permit light guidance in a hollow core by a photonic bandgap, which provides a paradigm shift in fiber optics, and has stimulated

Optical and Electronic Fibers: Emerging Applications and Technological Innovations, First Edition. Edited by Lei Wei.

important technological and scientific applications [3]. For example, PCFs have been implemented for in-line controlling the wavelength, modes, polarization, and orbital angular momentum of the light fields. There is continuous progress in designing the low-loss microstructured fibers for optical communications, and recently developed hollow-core conjoined-tube negative-curvature fiber shows the potential of low loss beyond the standard optical fibers [4].

The photonic integrations with small footprints are always in pursuit of goals for improved performance, power, volume, and cost. By tapering from the bulk fiber/materials, the miniaturized microfibers are demonstrated with many intriguing properties, such as the strong light field confinement, large surface evanescent fields, tunable dispersion, and mechanical configurability. These micro-/nano-scale waveguides bridge the fiber optics and nanotechnology for enhanced light–matter interactions. The mechanical flexibility and strength of microfibers also enable various photonic structures for the proposed sensing and optoelectronic applications [5–7]. On the other hand, the merging of materials and microstructures into a single fiber is proposed and demonstrated to realize optical, electronic, and mechanical functions that can sense and communicate. By sophisticatedly stacking multimaterials and co-drawing the preforms, they yield kilometers of functional fiber devices. While the multifunctional multimaterial fibers show the great potential of lab-on-fiber technology, there are very limited materials for joint integration, considering the interface-energy-driven capillary break-up effect [8]. Moreover, they are still challenging to be connected with the standard optical fiber systems with low loss for the intrinsic mode-field mismatch and splicing difficulty. As a result, there is a rising interest in hybrid integration of functional materials to the structured silica fiber platform by the well-developed post-processing techniques. In the beginning of the twenty-first century, the rise of Dirac fermionic graphene materials has attracted great research interest among many fields from the seminal work of Novoselov et al. [9]. Graphene is demonstrated with many fascinating properties, including the ultrahigh carrier mobility, thermal conductivity, broadband light absorption, and mechanical strength. The fast development of graphene-based 2D materials brings new opportunities in the fiber integration, as shown in Figure 1.1, since they have excellent optical and optoelectronic properties. The strong in-plane mechanical strength of the typical 2D materials with naturally passivated bonds enables the tight attachment to the fiber structures either in the flat or curved surface without the need for lattice match. Besides, the atomic thickness of 2D materials keeps the optical modes almost intact along with the enhanced light–matter interactions. Consequently, 2D materials can be fully complementary to the conventional passive silica fibers and achieve the functions of light emitting, modulating, sensing, and detecting.

The optical fiber integration with 2D materials for optics and optoelectronics is a highly interdisciplinary research field that includes condensed matter physics, optics, and mechanics. This field is still in its early stages of development, and there have been substantial advances recently. This chapter will first review the development of optical fibers. Second, the basic properties of mainstay 2D materials, i.e. graphene, transition metal dichalcogenides (TMDC), and black phosphorous (BP), and their heterostructures are introduced. Third, the 2D-materials-fiber design strategy and fabrications are described. Fourth, recent progress of fiber integrations for

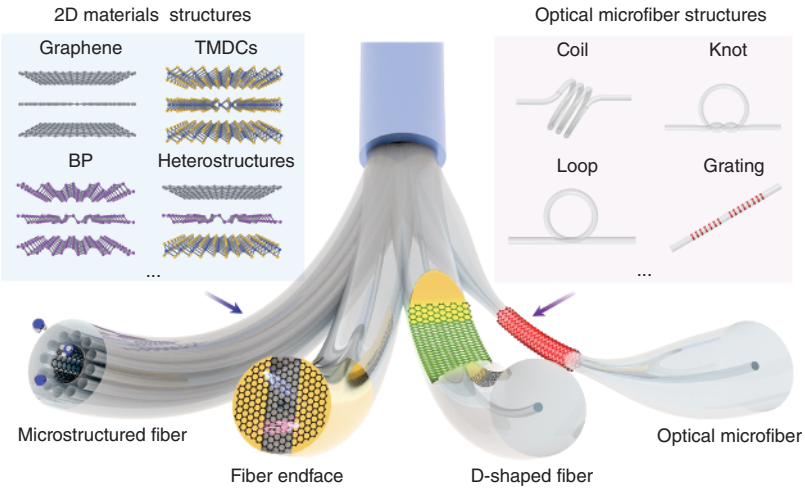

Figure 1.1 Schematic of 2D materials integration to optical fiber platform. TMDCs: transition metal dichalcogenides, BP: black phosphorous. Source: Chen et al. [10] / Springer Nature / CC BY 4.0.

optics and optoelectronics is discussed, mainly in the scope of polarimetric device, light sources, modulators, detectors, nonlinear optics, and fiber-optic sensors. Finally, the challenges and prospects of this field are briefly overlooked.

1.2 Fiber-integrated 2D Materials for Photonics and Optoelectronics

Basically, 2D materials are defined as crystalline materials composing single- or few-layer atoms, most of which are formed by the strong intralayer bonds and the weak interlayer van der Waals force. Benefited from the graphene research, the library of 2D materials is rapidly being increased from the mono-elements to compounds. Different from their three-dimensional (3D) counterparts, 2D materials can strongly interact with light, and their optical responses can be modulated with high flexibilities, such as by electrical gating, optical excitations, chemical doping, and strain gauge [10, 11]. Note that the fiber integration with 2D materials is still limited to a few mature 2D materials, and there is plenty of room to explore in this emerging field. As following, the basic optical and optoelectronic properties of the mainstay 2D materials are discussed.

1.2.1 Basic Properties of 2D Materials

1.2.1.1 Graphene

Monolayer graphene consists of carbon atoms arranged in a 2D honeycomb lattice, and each carbon atom is connected to the three nearest neighbors by a strong σ bond. Consequently, graphene shows an ultrahigh Young's modulus of ~1.0 TPa and

an intrinsic strength of 130 GPa [12]. Besides, the monolayer graphene is stable in oxygen atmosphere at temperatures up to 300 °C, and the multilayered samples can withstand ~500 °C without oxidation [13]. From the tight-binding model, the electronic band structures of graphene manifest the linear Dirac cones in the low-energy regime (Figure 1.2a), which leads to many intriguing electrical and optical properties [14]. For example, graphene has an ambipolar electric field effect with intrinsic carrier mobility reaching 10^6 cm^2/Vs. In optics, graphene has linear light absorption of approximately 2.3% per layer in the visible and near-infrared band (Figure 1.2b), defined by the fine structure constant [18]. More importantly, the light absorption can be readily tuned by the external fields such as electric gating, chemical doping, and strain. For nonlinear optics, the typical third-order nonlinearity ($\chi^{(3)}$) of graphene is as large as ~10^{-19} m^2/V^2, which is three orders of magnitude larger than that of fused silica. The ultrafast carrier relaxation of graphene has enabled the low-threshold saturable absorber and all-optical switch [19, 20]. In addition, the third harmonic generation (THG), four-wave mixing (FWM), saturable absorption (SA), and Kerr effect of graphene have been observed based on the third-order nonlinearity. It is revealed that the THG and FWM processes are highly dependent on the graphene Fermi level and the input light frequency [21]. The high harmonic generation (HHG) in graphene is observed and enhanced by elliptically polarized light excitation, which opens up the possibility of exploring strong-field and ultrafast nonlinear dynamics in massless Dirac fermions. Note that the intrinsic second-order nonlinearity is electric–dipole forbidden in perfect graphene films due to their centrosymmetry. Nevertheless, various methods have been proposed, such as applying strain, electric current, and chemical doping, to induce the second harmonic generation (SHG).

1.2.1.2 Transition Metal Dichalcogenides

The TMDCs, in the form of MX_2, where M is a transition metal atom (such as Mo and W) and X is a chalcogen atom (such as S, Se, or Te), have a long research history before the graphene discovery. Different from the gapless graphene, most of the TMDCs are semiconductors. Here, the MoS_2 or WS_2 are mainly introduced, and similar properties can be found in other TMDCs. The evolution of the band structures of MoS_2 is first studied, which reveals the transition from indirect bandgap to direct bandgap with the layer numbers (Figure 1.2c), because of the strong interlayer coupling [15, 22]. It is found that the photoluminescence quantum yield of a suspended monolayer MoS_2 is increased by four orders of magnitude compared with the bulk crystals [22]. The reduced dielectric screening and enhanced Coulomb interaction in TMDCs lead to the tightly bound excitons, charge excitons (trions), and biexcitons with large binding energies. For instance, the typical binding energies of A excitons in TMDCs are measured in the range of 0.2–0.8 eV. Thus, the optical properties of layered TMDCs are dominated by the excitonic effect and exhibit considerably strong light–matter interactions of light absorption up to ~20% in the visible/near-infrared spectra [23].

Another intriguing property of monolayer MoS_2 is the valleytronics. The monolayer MoS_2 is in trigonal prismatic (2H) phase, and the valence band maximum

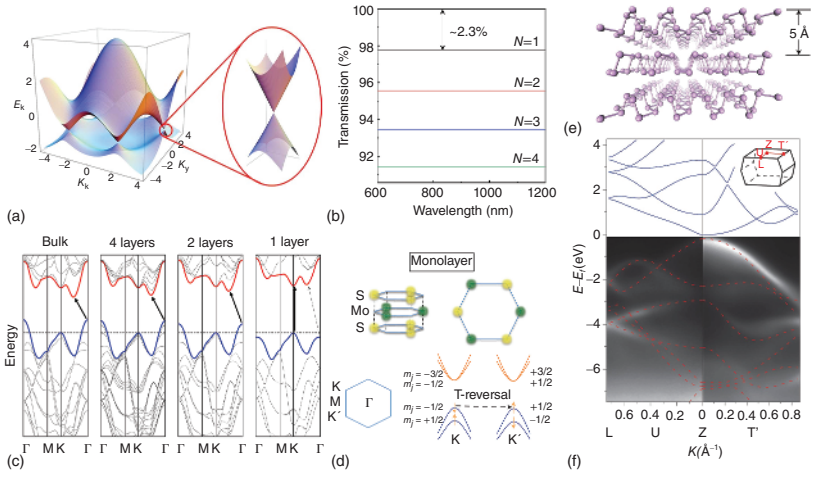

Figure 1.2 (a) The electronic band structures of monolayer graphene. Inset shows the Dirac cone structure at the edge of Brillouin zone [14]. (b) Calculated transmittance spectra of free-standing graphene (in air) of different layer numbers ($N = 1-4$). (c) Calculated band structures of 2H-MoS_2 for different layer numbers [15]. (d) Upper panel: the honeycomb lattice structures of monolayer MoS_2. Lower panel: the lowest-energy conduction bands and the highest-energy valence bands labeled by the z-component of their total angular momentum. The spin degeneracy at the valence-band edges is lifted by the spin–orbit interactions [16]. (e) Atomic structure of black phosphorus (BP) [17]. (f) Band structures of bulk BP mapped out by angle-resolved photoemission spectroscopy (ARPES) measurements [17]. Source: (a) Reproduced with permission from Neto et al. [14], American Physical Society. (c) Reproduced with permission from Splendiani et al. [15], American Chemical Society. (d) Reproduced with permission from Mak et al. [16], Springer Nature. (e, f) Reproduced with permission from Li et al. [17], Springer Nature.

and the conduction band minimum are located at the two inequivalent points K and K′. The inherent inversion symmetry breaking along with spin–orbit interactions contribute to coupled spin and valley physics in monolayer MoS_2 (Figure 1.2d) [16, 24], which are also observed in other group-VI dichalcogenides. The optical pumping of circular polarization is implemented to achieve complete dynamic valley polarization in monolayer MoS_2 [16], which has stimulated many valley-based optoelectronic applications in plasmonic, photonic crystal, and waveguide platforms. For nonlinear optics, the TMDCs have intrinsic second-order nonlinearity ($\chi^{(2)}$) due to the broken inversion symmetry. The typical $\chi^{(2)}$ of MoS_2 or WS_2 is reported to be ~1 nm/V, which is much higher than the commercial nonlinear crystals, such as $LiNbO_3$. Although the absolute conversion efficiency in most of the TMDCs devices is far less than the bulk crystals due to their atomically thin light–matter interactions, the unique tunability or modulation of TMDCs nonlinear optics by the excitonic effect, field effect, edge state, and stacking order can promise novel optoelectronic devices [25]. To boost the efficiency of SHG, the integration of TMDCs and photonic structures, such as plasmonic lattices, photonic crystals, Mie resonators, whispering gallery cavities, and optical waveguides, is demonstrated. The third-order nonlinear susceptibilities of MoS_2 is comparable to those of graphene,

and THG, SA, FWM , and two-photo absorption (TPA) are also extensively studied. Note that the TPA coefficient of monolayer MoS_2 is as high as 7.6×10^{-8} m/W, which is three orders of magnitude higher than that of the conventional semiconductors (GaAs, CdS, and ZnO) [26]. The nonperturbative HHG from a monolayer MoS_2 is demonstrated with even and odd harmonics up to the 13th order. The combination of strong many-body Coulomb interactions and tunable electronic properties in 2D materials provides a new testbed for attosecond science [27].

1.2.1.3 Black Phosphorus

The BP is a single-elemental layered orthorhombic material, in which the intralayer phosphorus atoms are arranged in a puckered honeycomb lattice, as shown in Figure 1.2e. The low-symmetry crystal structure of BP determines their strong anisotropy in both electrical and optical properties (Figure 1.2f), which are fundamentally different from the graphene and TMDCs (such as MoS_2 and WS_2). Since the first demonstration of few-layer BP transistors, BP has regenerated interest for its high carrier mobility (~1000 cm^2/V s) and on/off ratio (10^5) for devices of ~10 nm thickness at room temperature [17, 28]. In addition, BP fills the energy gap between graphene and TMDCs, and the strong interlayer coupling leads to the wide bandgap tunability with layer numbers. For example, the direct optical bandgap of bulk BP is ~0.35 eV, and it is increased up to ~1.73 eV for monolayer [29, 30]. Consequently, the thin BP film can cover wide optical spectra in visible, near-infrared, and mid-infrared, which indicates important applications in thermal imaging, optical communications, and medicine. Due to the puckered lattice structure, BP has demonstrated unique strain-dependent properties. For example, the bandgap of thin-film BP exhibits a modulation rate of 1.70 μm/% by strain covering 2.3–5.5 μm, which can be readily used to detect multiple gases such as CO_2, CH_4, and H_2O [31]. The widely gate-variable mid-infrared light emission in thin-film BP is also realized [32].

On the other hand, BP shows strong anisotropy in the optical properties. For example, the infrared and Raman spectroscopy reveal the linear-polarization-dependent response of BP, which can be implemented to characterize the crystal orientations and fabricate polarization-control devices. Intriguingly, the excitonic photoluminescence is highly polarized along the light effective-mass direction regardless of the input laser polarizations [33]. Recently, broadband electro-optic polarization conversion with tri-layer BP integrated in a Fabry–Pérot cavity is realized based on the strong birefringence effect [34]. For nonlinear optics, BP has comparable third-order nonlinearity (10^{-19} m^2/V^2) with graphene, and various nonlinear effects such as THG, FWM, and SA are reported. Note that although bulk BP is stable under ambient conditions, few-layer BP is found to degrade quickly in environments with oxygen, moisture, or at high temperatures (>60 °C). The physical coating materials such as graphene, aluminum oxide, polymethylmethacrylate (PMMA), and the covalent functionalizations are successfully utilized to suppress the oxidations at different time scales [35]. It is in great demand to improve the stability of BP for the ultimately practical applications.

1.2.1.4 Other 2D Materials and the Heterostructures

In recent years, the 2D materials research is rising quickly, and many different kinds of 2D materials are being discovered. It is predicted that more than 600 stable 2D materials exist, and there are still a plethora of opportunities to explore in 2D materials along with their heterostructures. On the other hand, researchers are tending to explore the specific materials with designed properties. For example, hexagonal boron nitride (hBN) is composed of boron and nitrogen atoms arranged in the honeycomb structures similar to graphene. The hBN has strong mechanical strength with chemical inertness, and it does not exhibit any optical absorption in the visible spectra due to the large bandgap in the ultraviolet (UV) range. Thus, hBN is very suitable as an encapsulating film or substrate for 2D material devices [36]. The group-IV monochalcogenides such as SnS, GeS, SnSe, and GeSe are isoelectronic with BP, and they have the orthorhombic structures. Due to the broken inversion symmetry, they feature spin-orbit splitting and piezoelectricity. They also show potential for valleytronics' applications for their twofold degenerate valence and conduction valleys, and the valley pairs can be selected using linear polarized light [36]. The natural layered oxides, i.e. α-MoO_3, are revealed to demonstrate phonon polaritons with elliptic and hyperbolic in-plane dispersion, which promises an unprecedented potential for the directional control of light in the mid-infrared spectra [37].

The hetero-integrations of semiconductors, dielectrics, or metals are essential for modern electronics and optoelectronics. In particular, integrating different materials with pristine interfaces is important for creating functional devices, which has been long pursuit of materials science and technology [36, 38]. The 2D materials offer a unique platform for assembling different materials in one vertical stack held by the weak van der Waals force, which is promising for the atomic-scale material design and application. The van der Waals integration is radically different from the conventional chemical epitaxial growth, such as molecular beam epitaxy or physical vapor deposition, which require the interfacial lattice match. When stacking different 2D layered materials together, many exciting demonstrations of proof-of-concept devices are realized, such the Moire lattices, surface reconstruction, atomic-layer light-emitting diodes, and tunneling devices [36]. Very recently, the magic-twist graphene layers are reported for superconductor and correlated insulator [39, 40], which open a new horizon in twisted van der Waals materials. Note that most of the 2D heterostructures are achieved in the planar substrate for condensed matter physics and optoelectronic applications; the optical fiber integration for the cutting-edge applications still remains to be explored.

1.2.2 Optical Fiber-2D-material Integrations

The unique structures of silica optical fibers determine that there is no universal strategy in fiber-2D-material integration. Overall, the conventional fiber structures mainly include fiber endface (tip), microfiber, D-shaped fiber (DSF), and microstructured fiber, and each has its own advantages and disadvantages for integration. The fiber

endface is an emerging microscopic platform for light–matter interactions, which shows miniature footprint and low insertion loss. Nevertheless, it suffers from the short light–matter interaction distance and small area. In the past years, many methods based on top-down or bottom-up techniques have been developed by the functional materials and photonics structures to enhance and manipulate the light fields on the fiber endface [41]. The fiber endface with 2D materials is straightforward, and the hybrid devices can be achieved by (polymer) film laminating, drop casting, and micro-transfer depending on the states of 2D materials. The hybrid graphene-fiber endface structure is first investigated for saturable absorption and used in ultrafast fiber lasers [19, 42]. Very recently, the van der Waals hetero-integration on fiber endface has attracted great attention and demonstrated applications in high-performance photodetection [43–45], chemical sensors [46], and polarimeters [47]. With the synergetic combinations of advanced photonic structures and 2D materials, it is promising to achieve novel all-fiber optoelectronics. On the other hand, the intriguing optomechanics of 2D materials can be interrogated on a fiber capillary tip, which can be used for all-fiber microelectromechanical system (MEMS) [48, 49].

Microfiber is a miniaturized optical fiber with diameters in the scale of the guided light wavelength, which is usually fabricated by flame tapering or chemical etching from a standard fiber (~125 μm). In the past years, optical microfibers have attracted interest for a range of photonic applications since they demonstrate many intriguing properties, such as strong field confinement, large evanescent fields, and structural reconfigurability [5]. For the hybrid integration, the 2D materials are conventionally deposited around the lateral wall of a microfiber by drop casting the nanoflakes solutions, which have important applications in optical sensors and saturable absorption for pulsed fiber lasers [50]. While more intriguing photonic applications are based on the intrinsic response of crystalline 2D materials integrated by either mechanical transfer or the chemical vapor deposition (CVD) method. For example, the ultrafast all-optical switch [20], tunable light absorption [51], reconfigurable exciton emission, and harmonic generations [52] have been demonstrated recently. On the other hand, the ingenious lab-on-a-rod technique realizes the 3D integration of coil microfiber and the functional materials or photonic structures onto a rod, as shown in Figure 1.3, which shows the great flexibility in tailoring light–2D materials interactions [54, 55] and can be applied for optical sensors, tunable fiber lasers, and polarimetric devices [53, 55–57].

The DSF structure is usually fabricated by mechanically polishing the side wall and exposing the fiber core, which can significantly enhance the surface evanescent interactions. The unique flat surface along the propagation in DSF not only enables the tight attachment of 2D materials but also increases the light–matter interaction length. The fabrication of hybrid DSF 2D materials is quite similar to that of the fiber endface, since both of them have the flat surfaces. The graphene–DSF is first reported for broadband fiber polarizer, and the high-performance all-optical modulator (AOM) [58], chemical sensors [59], and tunable fiber lasers [60] have been investigated recently. Microstructured optical fiber (MOF) with the air holes in the cladding or core region such as PCF is another emerging platform for accommodating 2D materials with potential of mass production. While MOF has been demonstrated to

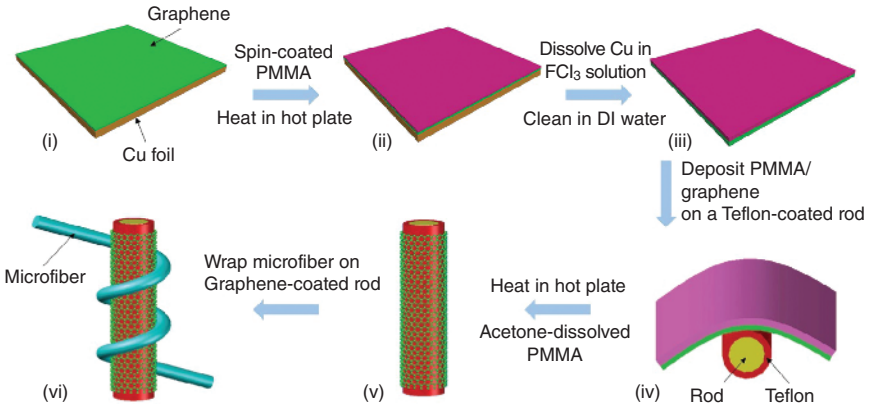

Figure 1.3 Fabrication process of the hybrid graphene-microfiber device. Panels (i)–(vi) demonstrate the detailed steps for transferring chemical-vapor-deposition growth graphene onto a surface modified rod (coated with low-index Teflon polymer), and panel 6 shows a schematic structure of the microfiber-on-graphene-rod device. Source: Reproduced from Chen et al. [53], Nature Publishing Group.

infiltrate gases, liquids, semiconductors, or metals for optoelectronics, it is a non-trivial task to fabricate high-quality 2D materials in their tiny microfluidic channels. Recently, a direct CVD-growth method was reported for the meter scale of graphene-PCF [61] and MoS_2-PCF production [62], which are applied for optical modulators and nonlinear optics. Note that different from the conventional multimaterial fibers, the atomic thickness of 2D materials keeps the optical modes of silica PCF intact and brings extraordinary optical functions. These works indicate the great potential for the ultimate commercial applications of all-fiber-2D-material devices.

1.2.3 Photonic and Optoelectronic Applications

In the past years, the fast development of hybrid fiber-2D-material integration has been witnessed, which has generated various novel fiber devices. In this section, recent development of fiber devices, i.e. polarimetric devices, light sources, modulators, photodetectors, nonlinear optics, and fiber-optic sensors, based on the 2D materials is discussed.

1.2.3.1 Polarimetric Devices

The optical polarizer is an optical filter that allows light waves of a specific polarization to pass through while blocking light waves of other polarizations. In fiber optics, an in-line fiber polarizer, based on polarization-selective coupling between evanescent fields and birefringent materials or plasmonic metals, has important applications in the coherent communication systems, optical gyroscopes, and interferometric sensors. Bao et al. [63] demonstrated the operation of a broadband polarizer in a graphene–DSF structure with an extinction of 27 dB, as shown in Figure 1.4a–c. The fiber polarizer showed much smaller loss in transverse-electric (TE) mode than in

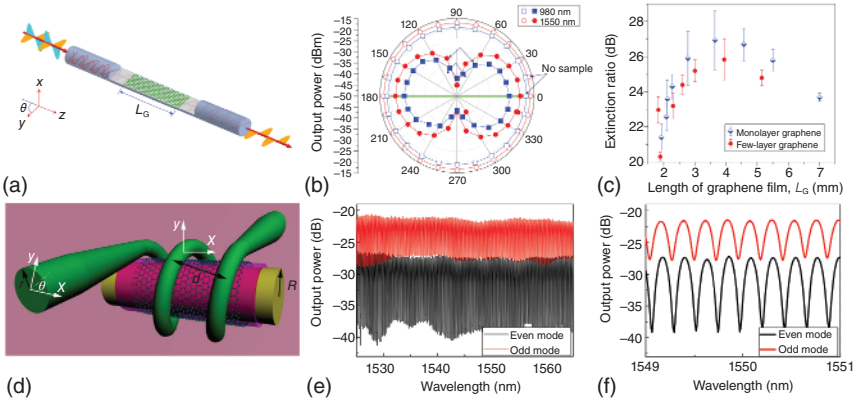

Figure 1.4 Polarimetric graphene-fiber devices. (a) Schematic model of graphene-D-shaped-fiber for polarizer. L_G, propagation distance (length of covered graphene film). Polarization angle θ is defined as the angle between the polarization direction of the analyzer (in x–y plane) and the graphene plane (y–z plane) [63]. (b) Polar image measured at 980 nm (L_G = 3 mm) and 1550 nm (L_G = 2.1 mm) [63]. (c) Polarization extinction ratio as a function of L_G measured at 1550 nm [63]. (d) Schematic structure of a stereo graphene-coil-microfiber in-line polarizer [55]. (e) Transmission spectra of the graphene-based resonator for two orthogonal modes [55]. (f) Enlarged view of the spectra at around 1550 nm from (e) [55]. Source: (a–c) Reproduced with permission from Bao et al. [63], Springer Nature. (d–f) Kou et al. [55] / Optical Society of America / CC BY 4.0.

transverse-magnetic (TM) mode since the graphene layer supported weakly damped TE mode. Different from the conventional fiber polarizer, the extinction ratios or even the polarization effect (TE-pass or TM-pass) in graphene polarizer is controllable by gate voltage (Fermi level) [60] or photon doping [53]. There are continuous efforts in optimizing the polarimetric performance through the polymer coating and structural modifications [64–66]. For example, Zhang et al. [65], reported a high extinction ratio of ~37.5 dB in the polymer–graphene–DSF structures with a low device loss ~1 dB. Kou et al. [55] presented a stereo graphene–coil–microfiber structure for polarization manipulation using a lab-on-a-rod technique (Figure 1.4d). Intriguingly, by tailoring the near-field coupling effect, they further demonstrated a high-Q single-polarization microresonator, which can be used for interferometric sensors with suppressed polarization cross-talk, as shown in Figure 1.4e–f. This design strategy can be readily used for other microfiber resonating structures. Recently, the 2D materials with strong optical dichroism effect such as ReS_2 and BP are investigated, and they show potential in polarimetric fiber devices [67].

1.2.3.2 Light Sources

The light-emitting devices are conventionally based on the direct radiation transition of carriers through the electrical or optical pumping. Consequently, the silica fiber (dielectric materials)-emitting devices require integrating external functional materials, such as semiconducting nanowires, quantum dots, rare earth ions, and fluorescence molecules. The emerging 2D materials with direct electronic bandgap

offer unique alternatives. There have been considerable advances of planar light-emitting devices based on TMDCs; on the contrast, the electrical pump light sources in fiber devices are lacking. Chen et al. [52] reported mechanical transfer of crystalline WS_2 film onto the surface of a submicrometer microfiber, and they observed enhanced excitonic absorption and emission in the evanescent-coupling configuration (Figure 1.5a), which is free from the limitations of the atomic thickness of WS_2. For example, the light absorption of the waveguide-coupled A-exciton was measured of ~97%, which was much larger than the free-space coupling of ~13%. From the in-fiber strain engineering, the peak wavelength of the photoluminescence and absorption spectra was dynamically tunable, as shown in Figure 1.5b,c; and this reconfigurable light source is difficult to achieve in conventional bulk materials. Liao et al. [69] investigated enhanced monolayer photoluminescence on silica micro-/nanofibers for low-threshold lasing. They found that the

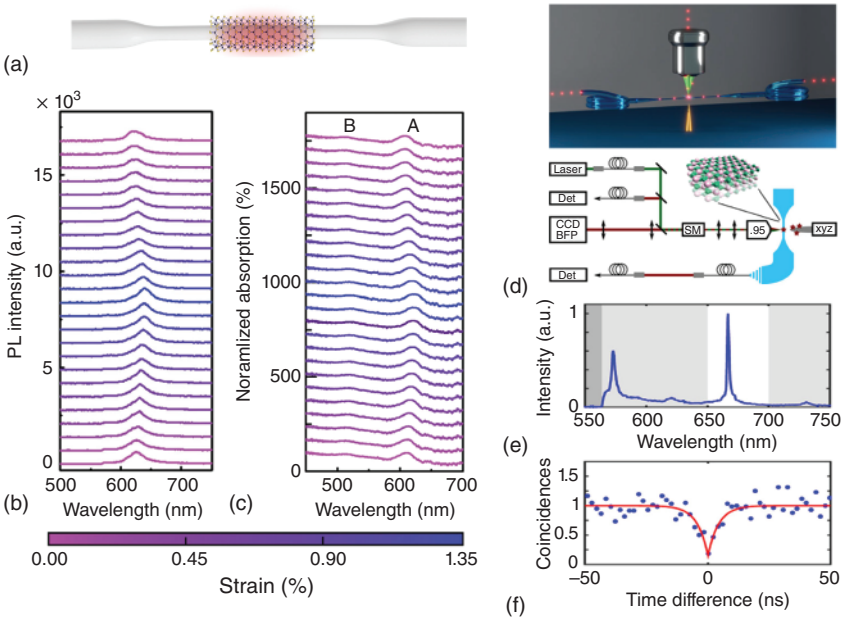

Figure 1.5 2D-materials-microfiber light emission sources. (a) Schematic hybrid WS_2-microfiber structure for enhanced light matter interactions [52]. In-line strain tuning of (b) the photoluminescence spectra and (c) absorption spectra of hybrid WS_2-microfiber. A and B are excitonic type of WS_2. (d) Upper panel: illustration of coupling quantum emitters in hBN to microfiber; lower panel: experimental setup. The experimental system consists of a homebuilt confocal microscope equipped with a piezo-driven three-axis manipulator (*xyz*) for attaching hBN flakes to a microfiber (colored blue). The microscope uses an objective lens with a numerical aperture of 0.95, and raster scanning is achieved using a scanning mirror assembly (SM) [68]. (e) Optical spectrum collected through the fiber, and (f) anti-bunching measurements of the light collected through the fiber. Value at zero time difference as extracted from the fits (red lines) is $g^{(2)}(0) = 0.15 \pm 0.20$ through the fiber [68]. Source: (a–c) Chen et al. [52] / Springer Nature / CC BY 4.0. (d–f) Reproduced with permission from Schell et al. [68], American Chemical Society.

high-density oxygen-dangling bonds released by photoactivation could be used to passivate the defects in MoS_2 or $MoSe_2$, and consequently improved the photoluminescence quantum yields. Furthermore, they demonstrated ultralow laser threshold of 5 W/cm^2 in MoS_2/microbottle device.

In addition to the classical light emission, a compelling aspect of the 2D materials is their applications for single-photon emitters (SPEs). The SPEs are isolated quantum systems that emit one photon at a time per excitation cycle, which can be triggered optically or electrically [70]. For the quantum science applications, the stable SPEs with high brightness, single-photon purity, and indistinguishability are in demand. The brightness of the SPEs characterizes the maximum single-photon emission rate. Single-photon purity represents the multiphoton emission probability, which can be quantified by the second-order autocorrelation function. The photon indistinguishability is conventionally characterized in the Hong–Ou–Mandel two-photon interference [71]. There are basically two kinds of SPEs in 2D materials, i.e. quantum dot (QD) and color center. The QD SPE originates from a bound exciton, which is confined in a potential formed by strain or crystallographic defect. The QD SPEs are first revealed in layered WSe_2 and are operated at cryogenic temperatures [72]. For the color-center type SPEs, they are impurities or point defects with electronic states that exist deeply in the bandgap. The hBN, as a wide bandgap material (~6 eV), can host a broad range of SPEs with zero phonon line emission ranging from the near-infrared to ultraviolet, and these SPEs can operate at room temperature. The integration of SPEs in fiber platform with high efficiency is a nontrivial task, since the deterministic optical mode coupling in the fiber waveguide can be further adapted in various photonic circuits. Schell et al. [68] demonstrated coupling of hBN-SPEs with a tapered microfiber, and they reached a collection efficiency of 10% in the hybrid fiber structure (Figure 1.5d,e). They found that the quantum nature of light was maintained throughout the fiber waveguide, as shown in Figure 1.5f. It is of great importance to exploit the SPEs that emit telecom band photons (~1.5 μm). Further, it is promising to further combine advanced fiber microstructures, such as gratings and resonators, and 2D materials engineering for the ultimate integrated SPEs of high brightness and purity.

1.2.3.3 Modulators

An optical modulator is a device used for controlling the amplitude, phase, or polarization state of a light beam. Based on the supreme optoelectronic functions of 2D material, the optical modulators have achieved substantial advances, which operate in the electromagnetic spectra spanning from ultraviolet to microwave. In this section, the fiber-integrated modulators for visible/infrared applications are discussed. In the past years, the all-optical modulator (AOM) and electric-optic modulator (EOM) have been extensively explored for their importance in optical communications network. The AOM uses a switching light beam to control the signal light beam, which can realize ultrafast modulation speed free from the electrical bottleneck. There have been various AOM devices designed based on Pauli-blocking effect, Kerr effect, and optothermal effect in 2D materials [10, 73], and their modulation bandwidth are different. Liu et al. [74] reported a graphene-covered-microfiber AOM device, with modulation

depth and speed to be 13 dB and 1 MHz, respectively. The moderate performance is probably limited by the quality of CVD-growth graphene and the large footprint of the device. Li et al. [20] showed an ultrafast graphene-clad microfiber with a modulation depth of 38% and a response time of ~2.2 ps (Figure 1.6a,b), approaching the intrinsic carrier relaxation time of graphene. This work unambiguously demonstrates the superiority of graphene-based modulators for optical signal processing. Later, Yu et al. [75] reported a graphene-clad microfiber with a Mach–Zehnder interferometer to covert Kerr phase shift to intensity modulation. This method can realize high modulation depth and optical transmission, avoiding the dilemma of a saturable absorption device, while the spectra bandwidth is compromised. Note that it is still challenging to handle and encapsulate such sub-wavelength microfiber (~1 μm diameter) for practical applications. Later, Chen et al. [53] proposed a robust stereocoiled graphene-microfiber structure for polarization-dependent light modulation with a maximized modulation of ~7.5 dB and a modulation efficiency of ~0.2 dB/mW. Zhang et al. [58] developed a polymer–graphene–DSF structure for enhanced modulation with an operation bandwidth of 0.5 THz. On the other hand, Gan et al. [76] demonstrated an all-fiber phase shifter and switch assisted by graphene's photothermal effect. They obtained a phase shift exceeding 21π with a nearly linear slope of 0.192 π/mW when pumped by 1540 nm

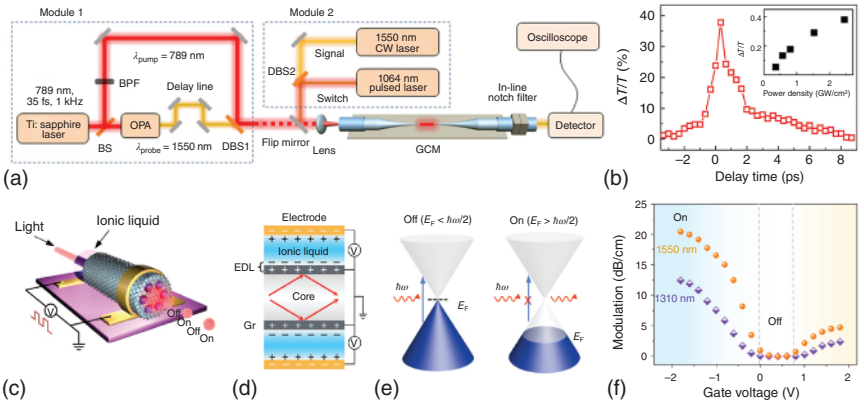

Figure 1.6 Optical fiber modulators with graphene integration. (a) Schematic illustration of experimental setups. Module 1: light source for pump–probe measurement. Module 2: light source for nanosecond-pulse modulation of a CW light [20]. (b) Differential transmittance of the probe light through a graphene-microfiber waveguide as a function of the pump–probe time delay. The inset shows the dependence of the modulation depth on pump intensity [20]. (c) Schematic of a graphene–PCF-based electro-optic modulator. The gate voltage between the ionic liquid and graphene controls light transmission through the graphene-PCF. (d, e) The working principle of the graphene–PCF electro-optic modulator, where an electrical double layer (EDL) forms at the interface between the graphene (dark gray rectangle) and ionic liquid (blue area). The ionic liquid-gating tunes the graphene's Fermi level and switches on and off the optical absorption in the graphene [61]. (f) Modulation curves at 1310 and 1550 nm show a transition between the "on" and "off" state with large modulation depth [61]. Source: (a, b) Reproduced with permission from Chen et al. [20], American Chemical Society. (c–f) Reproduced with permission from Chen et al. [61], Springer Nature.

light. Recently, there have been continuous advances in AOM devices beyond graphene, such as BP, TMDCs, and MXenes (transition metal carbides, carbonitrides, and nitrides). As for the ultimate commercial applications, the performance metrics of fiber AOM such as the control power consumption, switch time, and insertion loss are needed to be optimized and balanced [10]. In addition, the effective encapsulation of fiber devices is in demand.

The EOM is an optical device that implements direct-current (DC) or low-frequency electric field to control the light beams. There have been many advances in on-chip EOM based on graphene and other 2D materials [73]; on the contrast, the high performance of fiber-integrated EOM is less explored. Xu et al. [77] proposed a high-speed traveling-wave EOM based on a graphene/microfiber structure. The all-in-fiber electro-optic modulation was achieved by changing Fermi level of graphene, and $V\pi$ was designed of 4.9 V with 82 GHz 3 dB bandwidth. While, until now, the high-speed graphene-based fiber-EOM is not realized experimentally. Lee et al. [60] reported electrically tunable in-line graphene field effect transistors on a DSF. This device featured gate-variable electrical transport and optical transition at monolayer and multilayer graphene, and exhibited impressive optical transmission change >90%. Since the ionic liquid acts as efficient gating medium, this modulation speed is very slow. Chen et al. [61] demonstrated graphene-photonic-crystal-fiber with a length up to half a meter, which was produced using a modified CVD method. Similarly, they showed electrically gating graphene through an ionic liquid, with a large modulation depth of ~20 dB/cm at 1550 nm under a low gate voltage (~2 V), as shown in Figure 1.6c–f. For the high-speed applications, the adaptation of solid gating-dielectric and systematic circuit design is in demand [78, 79].

1.2.3.4 Photodetectors

Photodetectors are devices used for the detection of light or other electromagnetic radiation. In the fiber-optic systems, the transport light signals are usually out-coupled and detected by external bulk photodetectors based on various photoelectrical conversion mechanisms, such as photoconductive effect, photovoltaic effect, and photo-bolometric effect. The fast development of planar 2D-material-based photodetecting devices provides new opportunities and guidelines for fiber-integrated photodetectors. For the evanescent-field-coupling photodetectors, Sun et al. [80] reported broadband photodetection in a microfiber-graphene device, with a maximum photocurrent responsivity of ~2.81 mA/W in 1500–1600 nm. Jin et al. [81] investigated clean-transfer 2D InSe photodetectors onto a stripped fiber with a fast response time (~67 μs) and a responsivity of 769 mA/W (@~10 mW/cm^2). They also demonstrated a proof-of-concept in-line detection of a binary image signals. Recently, Zhuo et al. [82] demonstrated a hybrid carbon nanotubes (CNT)/graphene film in a DSF for enhanced responsivity of ~1.48×10^5 A/W (@0.23 μW/cm^2). On the other hand, there is an increasing interest in fiber endface photodetectors (FPD) for the simplified techniques and structural flexibility, as shown in Figure 1.7. Chen et al. [83] developed a mechanical scratch method to fabricate electrodes in fiber endface, and the few-layer MoS_2 was bonded to the silica substrate by van der Waals force. They measured a considerably high responsivity of

~600 mA/W (@5.5 mW/cm^2) at a bias of 4 V. Intriguingly, they also observed a responsivity of 10 mA/W under the bias-free conditions, which was attributed to the spatial asymmetry electrodes for the imbalanced photocarriers' transport. Later, they presented multi-materials integration by combining perovskite nanocrystals ($CsPbBr_3$) and multilayered graphene, and achieved a high responsivity of 2×10^4A/W (@75 μW/cm^2) with a power detection limit of 10^{-11} W [43]. Xiong et al. [44] reported a graphene–MoS_2–WS_2 heterostructure FPD with a synergetic photogating mechanism, as shown in Figure 1.7a. They found that the photodetectors exhibited an ultrahigh responsivity of ~6.6×10^7 A/W (@6.35 nW/cm^2) and a fast response time of ~7 ms at visible band. Moreover, they revealed that due to the type-II band alignments in MoS_2–WS_2, the photodetectors displayed a responsivity of ~17.1 A/W (@25.4 mW/cm^2) at 1550 nm. Recently, they demonstrated an ultracompact seven-core fiber De-multiplexer by integrating a patterned graphene photodetector array on a single-fiber endface [84], which shows great promise in multicore fiber optics.

In the past years, the figures of merit for fiber photodetectors are significantly improved, benefiting from the heterointegration strategy, as shown in Table 1.1. Nevertheless, the high-speed photodetecting components based on 2D-materials-fiber structure for GHz bandwidth are still lacking until now, which is highly in

Table 1.1 Figures of merit for 2D-materials-fiber photodetectors.

2D-Materials-fiber	V_{ds} (V)	λ (nm)	P (mW/cm^2)	Responsivity (mA/W)	Noise equivalent power (W/Hz$^{1/2}$)	Rise time (ms)	References
Graphene-microfiber	1	1550	9.0×10^6	2.81	~10^{-9}	—	[80]
InSe-microfiber	0.4	543	10–100	769	—	0.045	[81]
CNT/Graphene-DSF	0.3	1550	2.29×10^{-4}	1.48×10^8	6.76×10^{-12}	75	[82]
MoS_2-fiber endface	4	400	5.5	600	—	7.1×10^3	[83]
Graphene-$CsPbBr_3$-fiber endface	0.2	400	7.5×10^{-2}	2×10^7	3.9×10^{-16}	3.1×10^3	[43]
Graphene-MoS_2-WS_2-endface	−3	400	6.35×10^{-6}	6.6×10^{10}	—	7	[44]
		1550	25.4	1.71×10^4	—	10	
Graphene-COF-fiber endface	3	473	3.3×10^{-6}	3.2×10^{10}	~10^{-16}	1.14	[45]
BP-fiber endface	0.5	1550	~79	~8.52×10^3	~1.5×10^{-4}	8×10^{-4}	[47]

demand for the optical communication networks. In another aspect, researchers are exploring the cutting-edge applications of the developed fiber photodetectors. Xiong et al. [45] developed ultrahigh-responsivity photodetectors of 2D covalent organic frameworks (COFs) and graphene with a photoresponsivity of ~3.2×10^7 A/W. Based on the high surface area and the polarity selectivity of COFs, they demonstrated the gas sensing potentials with the fiber phototransitors, as shown in Figure 1.7b. Recently, Xiong et al. [47] for the first time demonstrated twisted BP-based van der Waals stacks for fiber-integrated polarimeters (Figure 1.7c). The real-time in-line detection of the light polarization is crucial in communication, imaging, and sensing fields. The conventional polarimeters use a series of opto-electro-mechanical elements, including lenses, polarizers, waveplates, and photodetectors, which are discretely arranged in an optical path and are highly cumbersome. Recent work ingeniously stacked three photodetection units based on six-layer van der Waals materials, including one isotropic Bi_2Se_3 for power calibration, two twisted BP layers for polarization detection, and three hBN for encapsulation. Intriguingly, the proposed device enabled polarimetric imaging to acquire spatial polarization information by Hadamard single-pixel imaging technique, as shown in Figure 1.7d [47]. The ultracompact device structure with the deterministic and accurate van der Waals materials integration, free from external optical and mechanical modules, may inspire the development of miniaturized optical and optoelectronic systems.

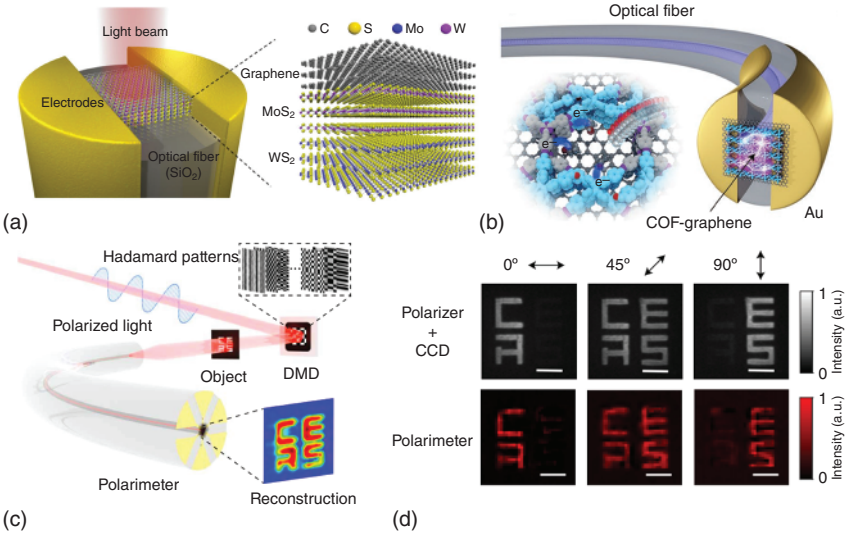

Figure 1.7 Optical fiber photodetectors with 2D-materials integrations. (a) Schematic view of the fiber endface photodetector (FPD) of the graphene-MoS_2-WS_2 heterostructure [44]. (b) Optoelectronic properties of FPD with of the covalent-organic-frameworks (COF) modified graphene film, regulated by gas molecules [45]. (c) Schematic of single-pixel polarimetric imaging by the FPD-based polarimeter. (d) Comparison of the images recorded by the CCD with a polarizer and the images (normalized intensity) reconstructed by the fiber polarimeter device under different linearly polarized illuminations [47]. Scale bars, 1 mm. Source: (a, b) Reproduced with permission from Xiong et al. [44, 45], JOHN WILEY & SONS, INC. (c, d) Reproduced with permission from Xiong et al. [47], American Association for the Advancement of Science - AAAS.

1.2.3.5 Nonlinear Optics

Nonlinear optics is the study of the intense light field in nonlinear media, where the optical response of materials responds nonlinearly to the electric field of light. The optical polarization $\boldsymbol{P}(t)$ of a material to the applied fields can be represented by a power series of the electric field strength $\boldsymbol{E}(t)$, as following:

$$\boldsymbol{P}(t) = \varepsilon_0 \left(\chi^{(1)} \boldsymbol{E}(t) + \chi^{(2)} \boldsymbol{E}(t)^2 + \chi^{(3)} \boldsymbol{E}(t)^3 + \cdots \right) \tag{1.1}$$

where ε_0 is the vacuum permittivity, $\chi^{(n)}$ is the nth order nonlinear susceptibility ($n \geq 2$), and $\chi^{(1)}$ is the linear susceptibility. From Eq. (1.1), it readily indicates that the nonlinear polarization terms can become significant when the light intensity is high. The typical nonlinear optical effects include second-order and third-order nonlinearity, which correspond to the second and third terms in the right side of Eq. (1.1), respectively. From the process of light–matter interactions, the nonlinear effects can also be classified as parametric and nonparametric processes. The parametric process indicates no occurrence of net transfer of energy or momentum between light field and the physical system [85], and it usually includes harmonic generations, sum/difference frequency generation, parametric oscillation, and optical Kerr effect, etc. On the contrast, the nonparametric process indicates that the quantum state of the medium is changed by the process, which includes Raman scattering, Brillouin scattering, two-photon absorption, saturable absorption (SA), and optical limiting, etc. In the past years, there is emerging research interest of 2D-materials nonlinear optics, since they have so many intriguing nonlinear optical properties, such as tunable nonlinearity from stacking order, strain and doping, phase-matching free by the atomic thickness and excitonic resonance [86]. Besides, the nonlinear spectroscopy has been shown to be an effective tool to characterize the fundamental properties of 2D materials. Considering the moderate nonlinear susceptibility of silica materials, for example, the small third-order nonlinearity and zero second-order nonlinearity from centrosymmetry, 2D materials integrations can go beyond the silica fiber nonlinear optics.

The SA is a third-order nonlinear effect of materials, where the light absorption is decreased with increasing light intensity (Figure 1.8a). The SA effect of graphene-based 2D materials has been extensively explored for pulsed fiber lasers spanning the spectra from visible to mid-infrared, along with the *Q*-switched or mode-locked state. In particular, the interplay of broadband gain media, SA effect, and the balance of linear and nonlinear effects in the fiber laser circuit can enable the ultrashort pulse duration. Bao et al. [19] showed that the modulation depth of light absorption could be tuned from 66.5% to 6.2% by varying the graphene layers, as shown in Figure 1.8b. They further reported the use of atomic-layer graphene in a mode-locked fiber laser (Figure 1.8c) for the generation of ultrashort soliton pulses (756 fs) at the telecommunication band. Sun et al. demonstrated a graphene–polymer composite for saturable absorber, and they showed a passively mode-locked fiber laser at 1559 nm, with 5.24 nm spectra bandwidth and ~460 fs pulse duration. Compared with commercial semiconductor saturable absorber mirrors (SESAMs), the graphene is shown to have an ultrawide spectra operation and tunable

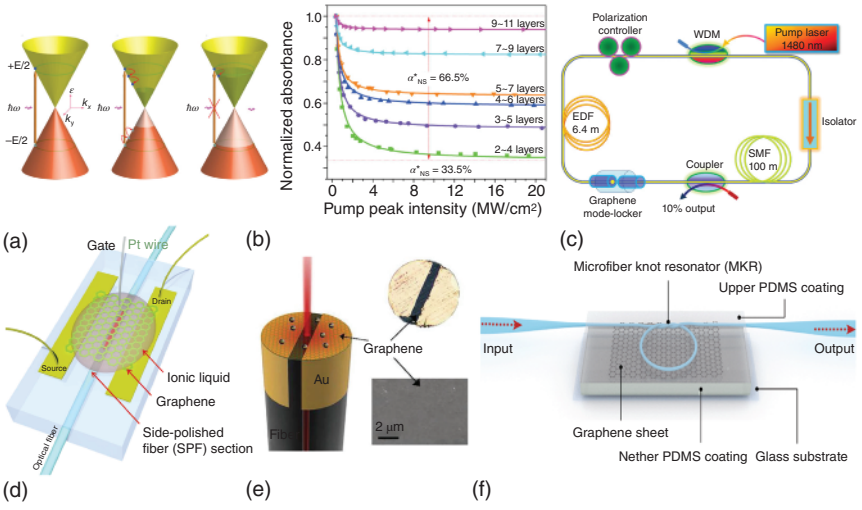

Figure 1.8 Optical fiber integrated with graphene saturable absorber. (a) Schematic of optical interband transition in graphene (left panel), the photogenerated carriers relaxation process (middle panel), and Pauli blocking effect at high excitation intensity (right panel) [19]. (b) Nonlinear absorption of graphene films with different number of layers [19]. (c) Laser configuration constituting a ring cavity. This schematic shows the standard fiber-optic components such as wavelength division multiplexer (WDM), polarization controller, coupler, optical isolator, erbium-doped fiber (EDF), and single-mode fiber (SMF) [19]. (d) Schematic diagram of gate-variable all-fiber graphene device [60]. (e) Schematic of graphene-fiber endface integration device, manipulating by electrical current induced Ohmic heat. Upper right panel shows the microscopic image of the sample. Lower right panel is the scanning electron microscope image of the graphene [87]. (f) Schematic of a high-*Q* microfiber ring resonator (with fiber pigtails) attached to multilayer graphene film and coated by PDMS [88]. Source: (a–c) Reproduced with permission from Bao et al. [19], JOHN WILEY & SONS, INC. (d) Lee et al. [60] / Springer Nature / CC BY 4.0. (e) Reproduced with permission from Li et al. [87], JOHN WILEY & SONS, INC. (f) Reproduced with permission from Ding et al. [89], Elsevier Ltd.

modulation depth, thus the output state of fiber lasers can be dynamically manipulated. Lee et al. [60] reported active control of transmission for graphene–DSF devices with electrical gating (Figure 1.8d), which enabled electrically tunable fiber laser at various operational regimes. Li et al. [87] proposed and demonstrated the state-variable fiber laser by thermally engineering the Fermi–Dirac distributions of graphene films on a fiber endface based on the simple Ohmic heating method, as shown in Figure 1.8e. Similarly, Qin et al. [88] demonstrated tunable laser microcomb dynamics by leveraging the electrical tunability of the graphene device incorporated in a fiber cavity. Recently, Ding et al. [89] realized a multifunctional all-fiber mode-locked laser based on a graphene-integrated polarization-dependent microfiber resonator (Figure 1.8f). They considered the SA mechanism, nonlinear polarization rotation effect, and high-*Q* knot resonator, and observed the *Q*-switched pulse, single soliton mode-locked pulse, harmonic mode-locked pulse, and high-repetition-rate dissipative-FWM pulse depending on the experimental conditions.

Inspired by the graphene research, many other 2D materials, such as BP, TMDCs, and MXenes, are revealed to have SA effect and thus can be used for pulsed fiber lasers. Note that most of the previous work focuses on the spectral and temporal properties (repetition rate and pulse duration) of fiber lasers depending on the various 2D materials and the fiber cavities, while the noise characteristics (intensity noise, timing jitter, and comb-line frequency noise) of the output fiber lasers are less investigated, which is important for optical science and photonic technology [90].

The waveguide-integrated 2D-materials for enhanced parametric processes are attracting attentions, since these nonlinear effects have broad applications in novel light sources, optical sensors, optical metrology, and signal processing. FWM is an intermodulation phenomenon from third-order nonlinearity, and it describes interactions between two and three wavelengths producing two or one new wavelengths. Wu et al. [91] demonstrated the cascaded FWM phenomenon with a large spectral range over 15 nm in a graphene-coated microfiber waveguide. Recently, An et al. [59] reported tunable FWM in graphene–DSF configuration for individual gas molecule detection (Figure 1.9a,b). They showed that the FWM conversion efficiency could change steeply when the graphene Fermi level was tuned approximately at 0.4 eV for ~1.5 μm pump and seed pulse. At this condition, the gas adsorption on graphene with modulated Fermi level would be sensitively detected from the Stokes light signal. SHG is a nonlinear optical process in which two photons with the same frequency are combined to generate a new photon with twice the energy of the initial photons. Chen et al. [52] systematically studied a hybrid WS_2-microfiber structure for broadband and tunable enhancement of light–matter interactions. Based on the high second-order nonlinearity of deposited WS_2, they showed that the SHG conversion in a modified microfiber was ~20 times larger than that of a bare microfiber (surface nonlinearity from symmetry-breaking). They also revealed the strong polarization-dependent SHG of hybrid waveguide due to the interactions between evanescent fields and WS_2, as shown in Figure 1.9c,d. Intriguingly, the dynamic control of SHG by strain gauge was also demonstrated based on the tuning of phase matching (Figure 1.9e), which can be applied for tunable visible light sources. Jiang et al. [92] reported high-efficiency SHG and sum-frequency generation in a microfiber assisted with few-layer GaSe with only submilliwatt continuous-wave pump lasers, and the SHG intensity was enhanced by more than four orders of magnitude. Recently, Li et al. [93] demonstrated deterministic all-optical generation and electrical control of multiple plasmon polaritons in a hybrid graphene-DSF via difference frequency generation. The electrically tunable Fermi level of graphene enables the generation of broadband plasmon polaritons, which provides a new way to high-speed logic operations.

Generally, 2D-material-enhanced optical nonlinearity depends on the trade-off between optical loss and interaction length. The unintentionally generated defects absorption/scattering during 2D materials transfer processes can significantly influence the ultimate nonlinear conversion efficiency in the post-processed fiber devices [10]. Zuo et al. developed a direct growth of MoS_2 onto the internal walls of a silica PCF [62]. By using the as-fabricated 25 cm long fiber, both the SHG and THG

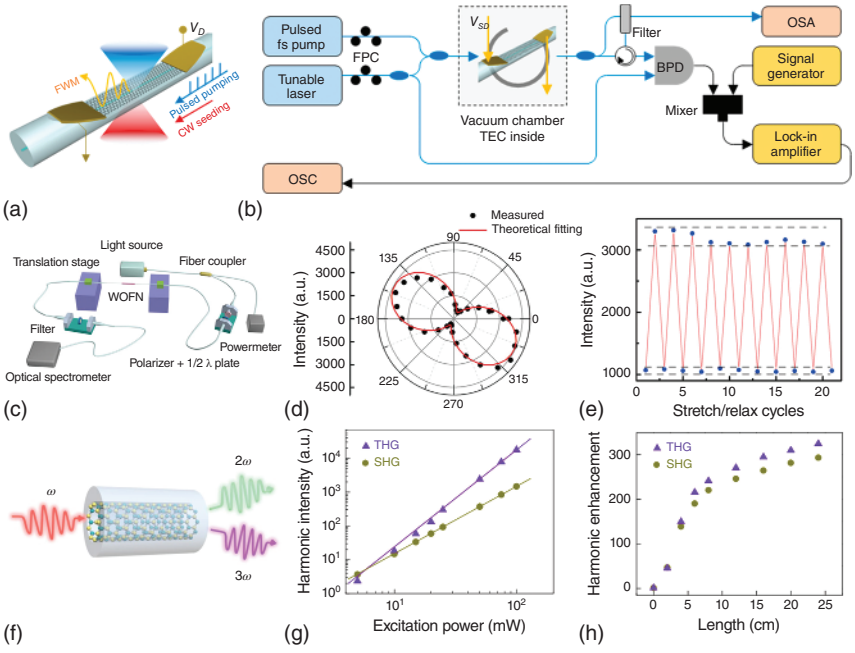

Figure 1.9 Optical fiber integrated with 2D materials for nonlinear optics. (a) Sketch of the electrically tunable four-wave-mixing (FWM) process in graphene–DSF [59]. (b) Experimental setup for gas sensing with based on gate-tunable FWM in graphene. BPD, balanced photodetector; OSA, optical spectrum analyzer; OSC, oscilloscope [59]. (c) Experimental setup for strain control of second harmonic generation (SHG) in the hybrid WS_2-microfiber [52]. WOFN: WS_2 optical fiber nanowire. (d) Polar image of the measured SHG intensity, as a function of the linear polarization of the pump light with a fixed input power [52]. (e) Cycling tests of strain modulation of the SHG of the WS_2-microfiber. Each stretch/relax step corresponds to a strain value of 0.45% [52]. (f) Schematics of SHG (2ω) and third harmonic generation (THG, 3ω) in MoS_2-embedded hollow-core fiber [62]. (g) Excitation-power dependence of SHG and THG intensities for MoS_2-HCF, showing the as-expected quadratic and cubic laws [62]. (h) Fiber-length-dependent SHG and THG enhancements in MoS_2-HCF with respect to MoS_2/silica, showing a general monotonic increase and saturation behavior with the fiber length [62]. Source: (a, b) An et al. [59] / American Chemical Society / CC BY 4.0. (c–e) Chen et al. [52] / Springer Nature / CC BY 4.0. (f–h) Reproduced with permission from Zuo et al. [62], Springer Nature.

were enhanced by ~300 times compared with monolayer MoS_2/silica, as shown in Figure 1.9f–h. This work shows the great potential of mass production of 2D materials fiber devices and can stimulate versatile nonlinear applications in the near future.

1.2.3.6 Fiber-optic Sensors

The fiber-optic sensor uses optical fibers as the sensing element, which exhibits many advantages over the electrical sensors, such as light weight, immune to electromagnetic interference, and remote sensing. In the past years, the 2D-material-integrated fiber-optic sensors attracted research interest, since the photonic/

optoelectronic properties of 2D materials can be strongly modulated by the external stimuli, which can be used to strengthen the performance of the silica fiber-optic sensors. Without loss of generality, here the graphene-based fiber sensors are focused in the scope of chemical and physical sensing, as shown in Table 1.2.

For chemical sensors, the graphene-fiber scheme has appealing features compared with the pure silica fiber structures, since graphene has ultrahigh surface-to-volume ratio, large adsorption capacity, and ultrafast carrier mobility [10, 102]. Generally, the adsorption of molecules changes the dielectric properties of graphene, which indirectly modulated the transported light fields by the amplitude, phase, polarization, or wavelengths. To achieve photonic resonance-enhanced sensing, researchers often integrate the graphene in the evanescent-coupling scheme of DSF, microfibers, gratings, interferometers, and cavities, as shown in Figure 1.10. Wu et al. [94] demonstrated an ultrasensitive gas sensor with a graphene-coated microfiber Bragg grating. They obtained sensitivities of −4 and 2 pm/ppm for NH_3 and xylene gas, respectively, which were 10 times larger than that of a bare microfiber grating. Similarly, Yao et al. [95] reported graphene-enhanced evanescent field in microfiber multimode interferometer (MMF) for gas sensing, and they achieved sensitivities of ~8 pm/ppm (~4 pm/ppm) for NH_3 (H_2O), which were 80 times higher than those of a bare MMF. Xiao et al. [98] studied reduced graphene

Table 1.2 Typical graphene-fiber sensors and their figures of merits.

2D-Materials-fiber	Sensing parameters	Maximal sensitivity	Detection limit	Response time	References
Graphene-microfiber-grating	NH_3	−4 pm/ppm	0.2 ppm	~5 min	[94]
	Xylene	2 pm/ppm	0.5 ppm	~10 min	
Graphene-multimode-microfiber	NH_3	8 pm/ppm	0.1 ppm	~1 s	[95]
	H_2O (vapor)	4 pm/ppm	0.2 ppm		
rGO-microfiber-grating	NO_2	~5 pm/ppm	0.5 ppm	~10 min	[96]
GO-long-period-fiber-grating	NO	~63.6 pm/ppm	0.36 ppm	23.6 min	[97]
Graphene-DSF	Humidity	0.31 dB/%RH	—	~15 s	[98]
Graphene-HCF	Refractive index	365.9 dB/RIU	2.73×10^{-6} RIU	—	[99]
Graphene-fiber-ferrule	Pressure	1.1 nm/Pa	~60 μPa/$Hz^{1/2}$[a]	—	[100]
MoS_2-fiber ferrule	Pressure	89.3 nm/Pa	—	—	[101]
Graphene-etched-fiber-tip	Electrical current	2.2×10^5 nm/A^2	0.3 mA	0.25 s	[48]
Graphene-coiled-microfiber	Electrical current	~6.7×10^4/A^2	0.5 mA	—	[56]

[a] Noise equivalent pressure.

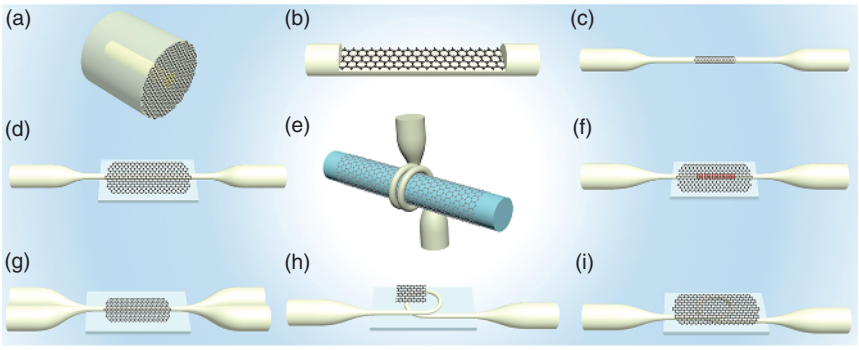

Figure 1.10 Typical optical microstructured fibers integrated with graphene-based 2D materials for sensors. (a–c) Graphene deposited on fiber endface, D-shaped fiber flat surface and tapered microfiber lateral wall. (d–g) Tapered microfiber on graphene substrate, coiled microfiber on graphene-coating rod, microfiber gratings on graphene and microfiber coupler on graphene substrate. (h, i) Microfiber ring partially and fully coated with graphene, respectively.

oxide (rGO)-coated DSF for humidity sensing with a sensitivity of 0.31 dB/% RH (relative humidity) in 75–95% RH (relative humidity). Huang et al. [99] reported plasma-enhanced CVD-growth graphene on hollow-core fibers (HCF), and they obtained a refractive sensitivity of 365.9 dB/RIU and a detection limit of 2.73×10^{-6} RIU. Xu et al. [97] reported ultrasensitive and selective detection of NO gas based on graphene oxide (GO)-coated long-period grating with a sensitivity of 63.6 pm/ppm. They showed that adsorption of NO molecules by GO was the combined effect of physical adsorption and chemical adsorption. In addition to the gases and vapors related sensors, the 2D-materials-fiber-optic sensors have been also implemented for detection of volatile organic compounds and heavy metal ions [103]. Note that there are continuous efforts to improve the chemical sensing sensitivity by optimizing the fiber structures and 2D materials (such as TMDCs, Mxenes, and BP); nevertheless, the sensing performance is fundamentally limited by the simply passive spectral sensing methods.

The active or nonlinear spectral sensing is promising for the ultimate single-molecule detection contributed by the high optical gain and electronic gain technique. Cao et al. [104] reported fluorescent resonance energy transfer in fiber-microfluidic resonator (Figure 1.11a). Besides, by measuring the intermode interference through noise-canceled beat notes and locked-in heterodyne detection with Hz-level precision, they achieved individual molecule sensitivity for dopamine, nicotine, and single-strand DNA detection. Yao et al. [105] demonstrated graphene-enhanced Brillouin optomechanical microresonator for ultrasensitive gas detection (Figure 1.11b,c). Theoretically, the molecular adsorption-induced surface elastic modulation in graphene enabled the Brillouin optomechanical modes extremely sensitive in NH_3 detection. They achieved a detection limit down to 1 ppb and an unprecedented dynamic range over five orders-of-magnitude. Note that the hybrid optical-electronic sensing

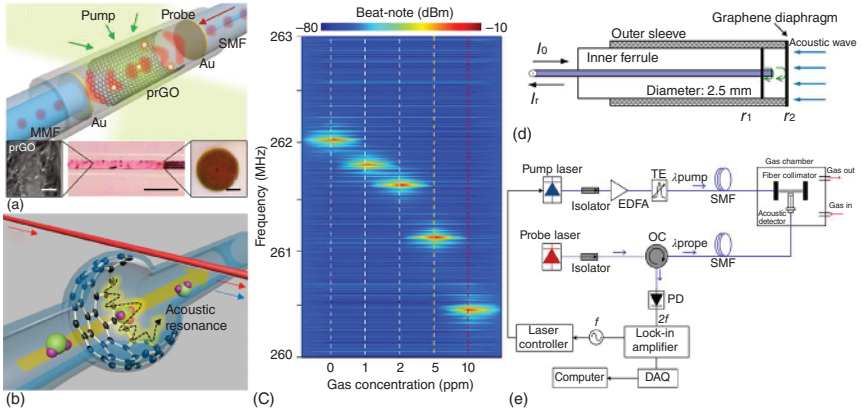

Figure 1.11 Active/nonlinear optical fiber-graphene device for ultrahigh sensitivity sensors. (a) Conceptual design and functionalization of the partially reduced graphene oxide (prGO) inner-deposited fiber sensor [104]. It composes two gold reflectors, prGO deposited inside-fiber, and Rhodamine 6G (Rh6G) as the optical-gain media. Inset from left-to-right shows the scanned electron micrograph of the prGO, the microscopic pictures of the resonator, and the fiber end with Au coverage. Inset scale bars from left-to-right are 2500 and 50 μm, respectively. (b) Schematic of graphene-enhanced Brillouin optomechanics of a microbubble cavity [104]. In this microcavity, the pump mode (red arrow) generates the Stokes mode (blue arrow) and the acoustic mechanical resonance mode (black arrow) [105]. (c) Colored map of the beat note spectra from the cavity optomechanical resonance, varies with the NH_3 gas concentration [104]. (d) Schematic of the fiber Fabry–Pérot interferometer with graphene diaphragm [106]. (e) Setup of photoacoustic spectroscopy system for acetylene detection [105]. Blue line, optical fiber; black line, electrical cable; TF, tunable filter; OC, optical circulator; PD, photo-detector; DAQ, data acquisition; DFB, distributed feedback laser (the pump); ECDL, external-cavity diode laser (the probe); EDFA, erbium-doped fiber amplifier. Source: (a) Cao et al. [104] / Springer Nature / CC BY 4.0. (b, c) Reproduced with permission from Yao et al. [105], American Chemical Society. (d, e) Reproduced with permission from Tan et al. [106], IEEE Publishing.

platform can obtain ultrahigh sensitivity, while the system complexity is also significantly increased compared with the conventional passive sensing methods.

For physical fields sensing, the 2D material-based MEMS are attracting great attention for their supreme optomechanical properties [12]. Ma et al. [49] reported a fiber-tip pressure sensor using a few-layer graphene as a diaphragm (diameter of 25 μm), which formed a low-finesse Fabry–Pérot (FP) interferometer. They realized a high pressure sensitivity over 39.4 nm/kPa. Further, they implemented multilayered graphene as a diaphragm of diameter 125 μm and obtained an improved pressure sensitivity of 1100 nm/kPa. They showed that this kind of graphene-FP cavity could be used for acoustic sensors, exhibiting a flat frequency response in the range of 0.2–22 kHz and a noise-equivalent acoustic single of ~60 $\mu Pa/Hz^{1/2}$ [100]. Later work showed that higher pressure sensitivity was achieved in few-layer MoS_2 diaphragm sensors, probably due to their relatively low Young's modulus of ~0.3 TPa and higher transferred film quality [101]. By integrating the metal electrodes on a fiber endface, Zheng et al. [48] demonstrated a miniature optical fiber current

sensor based on a quasi-static graphene MEMS, and they achieved simultaneously high sensitivity of 2.2×10^5 nm/A^2, a short response time of ~0.25 seconds, and a compact device size of ~15 μm. Besides the quasi-static-response MEMS applications, the intrinsic mechanical resonating properties by the clamped graphene membrane can enable the vibrational fiber-optic sensors for high-precision sensing measurements. For example, Tan et al. [106] reported using a graphene nanomechanical resonator as the acoustic detector, by operating the mechanical resonance of the graphene diaphragm, as shown in Figure 1.11d,e. The sensitivity for acoustic detection was enhanced, and a noise equivalent pressure of 2.11 μPa/Hz$^{1/2}$ was demonstrated. They further presented detection of acetylene gas and achieved a detection limit of 119.8 ppb with 123.9 mW pump power. It is promising to improve the performance of fiber-2D materials-MEMS by optimizing the 2D materials' quality and geometrical structures, and manipulating the pre-stress in fiber devices [10].

1.3 Conclusion

In this chapter, we have reviewed the basic optical properties of several mainstream 2D materials and their integrations to silica optical fibers for advanced optics and optoelectronics applications. We lay emphasis on the optical fiber devices for light field generation, modulation, and detection. Currently, most of the applications remain as proof-of-concept demonstrations, and the issues to realize scalable production with reliable packaging are waiting to be solved before any commercial implement. Recent development of CVD-growth method to produce polycrystalline 2D materials [61, 62], for example graphene and MoS_2 in hollow-core PCF, has provided a unique way to the massive production of hybrid fiber-2D-material devices. As for the future development of fiber-2D-materials integrations, more cutting-edge applications are in demand to explore by merging the extraordinarily properties/functions of 2D materials and the advanced photonic structures. In addition to the classical optics applications, it is very promising to explore the quantum optics in 2D materials for fiber-integrated quantum sources and even the quantum information processing.

References

1 Kao, K.C. and Hockham, G.A. (1966). *Proc. Inst. Electr. Eng.* 113: 1151–1158.
2 Peng, G.-D. (ed.) (2019). *Handbook of Optical Fibers*. Springer.
3 Russell, P. (2003). *Science* 299: 358.
4 Gao, S.-F., Wang, Y.-Y., Ding, W. et al. (2018). *Nat. Commun.* 9: 2828.
5 Brambilla, G., Xu, F., Horak, P. et al. (2009). *Adv. Opt. Photon.* 1: 107.
6 Chen, J.-H., Li, D.-R., and Xu, F. (2019). *J. Lightwave Technol.* 37: 2577.
7 Zhang, L., Tang, Y., and Tong, L. (2020). *iScience* 23: 100810.
8 Abouraddy, A.F., Bayindir, M., Benoit, G. et al. (2007). *Nat. Mater.* 6: 336.
9 Novoselov, K.S., Geim, A.K., Morozov, S.V. et al. (2004). *Science* 306: 666.

10 Chen, J.-H., Xiong, Y.-F., Xu, F., and Lu, Y.-Q. (2021). *Light Sci. Appl.* 10: 78.
11 Dai, Z., Hu, G., Ou, Q. et al. (2020). *Chem. Rev.* 120: 6197.
12 Lee, C., Wei, X., Kysar, J.W., and Hone, J. (2008). *Science* 321: 385.
13 Liu, L., Ryu, S., Tomasik, M.R. et al. (2008). *Nano Lett.* 8: 1965.
14 Neto, A.C., Guinea, F., Peres, N.M. et al. (2009). *Rev. Mod. Phys.* 81: 109.
15 Splendiani, A., Sun, L., Zhang, Y. et al. (2010). *Nano Lett.* 10: 1271.
16 Mak, K.F., He, K., Shan, J., and Heinz, T.F. (2012). *Nat. Nanotechnol.* 7: 494.
17 Li, L., Yu, Y., Ye, G.J. et al. (2014). *Nat. Nanotechnol.* 9: 372.
18 Nair, R.R., Blake, P., Grigorenko, A.N. et al. (2008). *Science* 320: 1308.
19 Bao, Q., Zhang, H., Wang, Y. et al. (2009). *Adv. Funct. Mater.* 19: 3077.
20 Li, W., Chen, B., Meng, C. et al. (2014). *Nano Lett.* 14: 955.
21 Jiang, T., Huang, D., Cheng, J. et al. (2018). *Nat. Photonics* 12: 430.
22 Mak, K.F., Lee, C., Hone, J. et al. (2010). *Phys. Rev. Lett.* 105: 136805.
23 Li, Y., Chernikov, A., Zhang, X. et al. (2014). *Phys. Rev. B* 90: 205422.
24 Xiao, D., Liu, G.-B., Feng, W. et al. (2012). *Phys. Rev. Lett.* 108: 196802.
25 Wen, X., Gong, Z., and Li, D. (2019). *InfoMat* 1: 317.
26 Li, Y., Dong, N., Zhang, S. et al. (2015). *Laser Photonics Rev.* 9: 427.
27 Liu, H., Li, Y., You, Y.S. et al. (2017). *Nat. Phys.* 13: 262.
28 Ling, X., Wang, H., Huang, S. et al. (2015). *Proc. Natl. Acad. Sci.* 112: 4523.
29 Yang, J., Xu, R., Pei, J. et al. (2015). *Light Sci. Appl.* 4: e312.
30 Li, L., Kim, J., Jin, C. et al. (2017). *Nat. Nanotechnol.* 12: 21.
31 Kim, H., Uddin, S.Z., Lien, D.-H. et al. (2021). *Nature* 596: 232.
32 Chen, C., Lu, X., Deng, B. et al. (2020). *Sci. Adv.* 6: eaay6134.
33 Wang, X., Jones, A.M., Seyler, K.L. et al. (2015). *Nat. Nanotechnol.* 10: 517.
34 Biswas, S., Grajower, M.Y., Watanabe, K. et al. (2021). *Science* 374: 448.
35 Wang, X. and Lan, S. (2016). *Adv. Opt. Photon.* 8: 618.
36 Novoselov, K.S., Mishchenko, A., Carvalho, A., and Castro Neto, A.H. (2016). *Science* 353: aac9439.
37 Ma, W., Shabbir, B., Ou, Q. et al. (2020). *InfoMat* 2: 777.
38 Liu, Y., Huang, Y., and Duan, X. (2019). *Nature* 567: 323.
39 Cao, Y., Fatemi, V., Fang, S. et al. (2018). *Nature* 556: 43.
40 Cao, Y., Fatemi, V., Fang, S. et al. (2018). *Nature* 556: 80.
41 Xiong, Y. and Xu, F. (2020). *Adv. Photonics* 2: 064001.
42 Sun, Z., Hasan, T., Torrisi, F. et al. (2010). *ACS Nano* 4: 803.
43 Chen, J.-H., Jing, Q., Xu, F., and Lu, Y.-Q. (2017). *Optica* 4: 835.
44 Xiong, Y.-F., Chen, J.-H., Lu, Y.-Q., and Xu, F. (2019). *Adv. Electron. Mater.* 5: 1800562.
45 Xiong, Y., Liao, Q., Huang, Z. et al. (2020). *Adv. Mater.* 32: 1907242.
46 Wang, H., Xiong, Y., Wu, C. et al. (2022). *Opt. Express* 30: 6818.
47 Xiong, Y., Wang, Y., Zhu, R. et al. (2022). *Sci. Adv.* 8: eabo0375.
48 Zheng, B.-C., Yan, S.-C., Chen, J.-H. et al. (2015). *Laser Photonics Rev.* 9: 517.
49 Ma, J., Jin, W., Ho, H.L., and Dai, J.Y. (2012). *Opt. Lett.* 37: 2493.
50 Luo, Z.-C., Liu, M., Guo, Z.-N. et al. (2015). *Opt. Express* 23: 20030.
51 Chen, J.-H., Luo, W., Chen, Z.-X. et al. (2016). *Adv. Opt. Mater.* 4: 853.
52 Chen, J.-H., Tan, J., Wu, G.-X. et al. (2019). *Light Sci. Appl.* 8: 8.

53 Chen, J.-H., Zheng, B.-C., Shao, G.-H. et al. (2015). *Light Sci. Appl.* 4: e360.
54 Xu, F., Horak, P., and Brambilla, G. (2007). *Opt. Express* 15: 7888.
55 Kou, J.-L., Chen, J.-H., Chen, Y. et al. (2014). *Optica* 1: 307.
56 Yan, S.-C., Zheng, B.-C., Chen, J.-H. et al. (2015). *Appl. Phys. Lett.* 107: 053502.
57 Li, C., Chen, J., Yan, S. et al. (2016). *IEEE Photon. J.* 8: 1500307.
58 Zhang, H., Healy, N., Shen, L. et al. (2016). *Sci. Rep.* 6: 23512.
59 An, N., Tan, T., Peng, Z. et al. (2020). *Nano Lett.* 20: 6473.
60 Lee, E.J., Choi, S.Y., Jeong, H. et al. (2015). *Nat. Commun.* 6: 6851.
61 Chen, K., Zhou, X., Cheng, X. et al. (2019). *Nat. Photonics* 13: 754.
62 Zuo, Y., Yu, W., Liu, C. et al. (2020). *Nat. Nanotechnol.* 15: 987.
63 Bao, Q., Zhang, H., Wang, B. et al. (2011). *Nat. Photonics* 5: 411.
64 Kim, J.T. and Choi, C.-G. (2012). *Opt. Express* 20: 3556.
65 Zhang, H., Healy, N., Shen, L. et al. (2016). *J. Lightwave Technol.* 34: 3563.
66 Chu, R., Guan, C., Yang, J. et al. (2017). *Opt. Express* 25: 13278.
67 Cui, Y., Lu, F., and Liu, X. (2017). *Sci. Rep.* 7: 40080.
68 Schell, A.W., Takashima, H., Tran, T.T. et al. (2017). *ACS Photonics* 4: 761.
69 Liao, F., Yu, J., Gu, Z. et al. (2019). *Sci. Adv.* 5: eaax7398.
70 Toth, M. and Aharonovich, I. (2019). *Annu. Rev. Phys. Chem.* 70: 123.
71 Aharonovich, I., Englund, D., and Toth, M. (2016). *Nat. Photonics* 10: 631.
72 He, Y.-M., Clark, G., Schaibley, J.R. et al. (2015). *Nat. Nanotechnol.* 10: 497.
73 Yu, S., Wu, X., Wang, Y. et al. (2017). *Adv. Mater.* 29: 1606128.
74 Liu, Z.-B., Feng, M., Jiang, W.-S. et al. (2013). *Laser Phys. Lett.* 10: 065901.
75 Yu, S., Wu, X., Chen, K. et al. (2016). *Optica* 3: 541.
76 Gan, X., Zhao, C., Wang, Y. et al. (2015). *Optica* 2: 468.
77 Xu, K., Xie, Y., Xie, H. et al. (2018). *J. Lightwave Technol.* 36: 4730.
78 Dong, L., Liu, X., Zhang, Y. et al. (2020). *ACS Appl. Electron. Mater.* 2: 447.
79 Cheng, X., Zhou, X., Tao, L. et al. (2020). *Nanoscale* 12: 14472.
80 Sun, X., Qiu, C., Wu, J. et al. (2015). *Opt. Express* 23: 25209.
81 Jin, Z., Ye, F., Zhang, X. et al. (2018). *ACS Nano* 12: 12571.
82 Zhuo, L., Fan, P., Zhang, S. et al. (2020). *Nanoscale* 12: 14188.
83 Chen, J.-H., Liang, Z.-H., Yuan, L.-R. et al. (2017). *Nanoscale* 9: 3424.
84 Xiong, Y., Xu, H., Wang, Y. et al. (2022). *ACS Photonics* 9: 1808.
85 Boyd, R.W. (2020). *Nonlinear Optics*. Academic Press.
86 Autere, A., Jussila, H., Dai, Y. et al. (2018). *Adv. Mater.* 30: 1705963.
87 Li, C., Chen, J.-H., Wang, W.-S. et al. (2017). *Adv. Opt. Mater.* 5: 1700630.
88 Qin, C., Jia, K., Li, Q. et al. (2020). *Light Sci. Appl.* 9: 185.
89 Ding, Z.-X., Chen, Y., and Xu, F. (2021). *Opt. Laser Technol.* 143: 107381.
90 Kim, J. and Song, Y. (2016). *Adv. Opt. Photonics* 8: 465.
91 Wu, Y., Yao, B.C., Feng, Q.Y. et al. (2015). *Photonics Res.* 3: A64.
92 Jiang, B., Hao, Z., Ji, Y. et al. (2020). *Light Sci. Appl.* 9: 63.
93 Li, Y., An, A., Lu, Z. et al. (2022). *Nat. Commun.* 13: 3138.
94 Wu, Y., Yao, B., Zhang, A. et al. (2014). *Opt. Lett.* 39: 1235.
95 Yao, B.C., Wu, Y., Zhang, A.Q. et al. (2014). *Opt. Express* 22: 28154.
96 Sridevi, S., Vasu, K., Bhat, N. et al. (2016). *Sens. Actuators, B* 223: 481.
97 Xu, B., Huang, J., Xu, X. et al. (2019). *ACS Appl. Mater. Interfaces* 11: 40868.

98 Xiao, Y., Zhang, J., Cai, X. et al. (2014). *Opt. Express* 22: 31555.
99 Huang, M., Yang, C., Sun, B. et al. (2018). *Opt. Express* 26: 3098.
100 Ma, J., Xuan, H., Ho, H.L. et al. (2013). *IEEE Photon. Technol. Lett.* 25: 932.
101 Yu, F., Liu, Q., Gan, X. et al. (2017). *Adv. Mater.* 29: 1603266.
102 Shivananju, B.N., Yu, W., Liu, Y. et al. (2017). *Adv. Funct. Mater.* 27: 1603918.
103 Pawar, D. and Kale, S.N. (2019). *Microchim. Acta* 186: 253.
104 Cao, Z., Yao, B., Qin, C. et al. (2019). *Light Sci. Appl.* 8: 107.
105 Yao, B., Yu, C., Wu, Y. et al. (2017). *Nano Lett.* 17: 4996.
106 Tan, Y., Zhang, C., Jin, W. et al. (2017). *IEEE J. Sel. Top. Quantum Electron.* 23: 199.